



HAL
open science

Inversion of Eddy-Current Signals Using a Level-Set Method and Block Krylov Solvers

Lorenzo Audibert, Hugo Girardon, Houssein Haddar, Pierre Jolivet

► **To cite this version:**

Lorenzo Audibert, Hugo Girardon, Houssein Haddar, Pierre Jolivet. Inversion of Eddy-Current Signals Using a Level-Set Method and Block Krylov Solvers. 2020. hal-03043491v1

HAL Id: hal-03043491

<https://hal.science/hal-03043491v1>

Preprint submitted on 7 Dec 2020 (v1), last revised 3 Aug 2021 (v2)

HAL is a multi-disciplinary open access archive for the deposit and dissemination of scientific research documents, whether they are published or not. The documents may come from teaching and research institutions in France or abroad, or from public or private research centers.

L'archive ouverte pluridisciplinaire **HAL**, est destinée au dépôt et à la diffusion de documents scientifiques de niveau recherche, publiés ou non, émanant des établissements d'enseignement et de recherche français ou étrangers, des laboratoires publics ou privés.

1 **INVERSION OF EDDY-CURRENT SIGNALS USING A LEVEL-SET**
2 **METHOD AND BLOCK KRYLOV SOLVERS***

3 LORENZO AUDIBERT^{†‡}, HUGO GIRARDON^{§‡}, HOUSSEM HADDAR^{‡§}, AND PIERRE
4 JOLIVET[¶]

5 **Abstract.** The application motivating this work is related to the identification of deposits inside
6 nuclear power plant steam generators using eddy-current probes. We consider a realistic experimental
7 process that relies on the scan of a domain by sweeping along a tube axis a probe made out of coils,
8 playing the role of the sources/receivers. Solving the inverse shape problem associated with these
9 measurements using a least squares method requires solutions to the eddy-current and the adjoint
10 problems for a large number of right-hand sides at each gradient-descent iteration. Additional cost
11 in the forward solver comes from the use of a potential formulation of the problem that has the
12 advantage of being independent from the topology of the conductive media (that may vary during
13 iterations). We use a level-set approach to avoid remeshing and handle unknown topologies. The
14 crucial ingredient in our algorithm is an optimized way of handling high numbers of right-hand sides
15 for iterative solvers of large-scale problems. We first benchmark various block Krylov methods, block
16 GMRES and block BGCRODR, to test their effectiveness compared to their standard counterpart,
17 i.e., GMRES and GCRODR. Then, we propose for BGCRODR a new implementation for recycling
18 information from previously generated Krylov bases that scales better than traditional approaches.
19 This part is independent from the practical inverse problem at hand. The efficiency of the overall
20 inversion procedure is finally demonstrated on realistic synthetic 3D examples.

21 **Key words.** eddy currents, domain decomposition preconditioners, block Krylov methods,
22 large-scale inverse problems

23 **AMS subject classifications.** 35Q61, 49Q10, 78A46, 65F10

24 **1. Introduction.** Nuclear power plants are thermal power plants using nuclear
25 fuel to produce electricity: heat gave off by the nuclear reaction is transferred by water
26 to a steam generator (SG) where it is used to vaporize colder water. The resulting
27 vapor goes through a turbine to generate electricity. The focus here is the SG where
28 hot water vaporizes cold water: it is composed of U-shaped tubes where hot water
29 flows. These tubes are plunged inside cold water. Contact with the heated tube wall
30 vaporizes the cold water: the vapor then streams upwards to the turbines. Over the
31 course of the operation, the cold water creates metallic deposits on the tube outer
32 wall [29]. These deposits deteriorate heat transfer on the tube [13], alter the flow of
33 the water and may create additional mechanical constraints on the device: detection
34 of such deposits is essential for the nuclear plant operator.

35 As direct inspection is impossible, indirect methods are used. Since the deposit
36 and the tube inside the SG are conductive, eddy-current testing (ECT) constitutes
37 the most suitable approach. ECT can be applied to different problematics, for in-
38 stance, crack detection inside SG [26, 24] or in a different setting [14], or paired with
39 thermography by using Joule effect [40]. The detection process using ECT is the
40 following. After emptying the device from the water, probes are inserted from one
41 end to the other end of a tube. By pulling them out at a constant speed, the operator
42 is able to make measurements at regular positions alongside the tube. The resulting
43 signal contains information on the medium configuration and, after post-processing,

*Submitted to the editors DATE.

[†]PRISME, EDF R&D, France

[‡]D&FI, INRIA Saclay, France

[§]mmAP, École Polytechnique, France

[¶]IRIT-ENSEEIH, CNRS, France

44 provides elements on the shape and position of deposits.

45 The probes are composed of a given set of coils: when a coil, called the emitter, is
 46 subject to a current, it produces an incident electromagnetic field. On the surface of
 47 conductive materials, eddy currents generate another electromagnetic field, disturbing
 48 the former. Another coil, called the receiver, then measures the flow of the distorted
 49 field and compares it to that of the incident field: the difference of flows is called
 50 impedance.

51

52 We propose to analyze the signals using an inverse shape problem approach. We
 53 formulate the inverse problem using a classical least squares functional and solve the
 54 resulting optimization problem using a gradient descent with adjoint state approach as
 55 in [17, 30]. These latter employ a boundary variation method or parametric encoding
 56 of the geometry to update the shape boundary. In this paper however, we choose to
 57 implicitly model the shape using a level-set function. The use of level-set functions in
 58 shape optimization is widespread in recent papers, for instance in optimal structure
 59 conceptions [39, 1], in electromagnetic inverse scattering [12], in optical tomography
 60 [34], or in fluid mechanics [25]. It handles more easily topological changes in the shape
 61 like merging or splitting in two connected components, while at the same time reduces
 62 computational costs compared to a boundary variation approach as the shape update
 63 does not require to re-mesh the computational domain anymore. We here adapt the
 64 level-set approach to the inverse problem at hand, introducing a regularization of the
 65 gradient descent and decoupling the mesh for the level-set function from the mesh for
 66 computing the solution of the forward problem.

67 Computation of an impedance signal for a given configuration requires the solu-
 68 tion of 3D time-harmonic Maxwell equations under the eddy-current approximation.
 69 Since the level-set approach may lead during iterations to complex topologies of the
 70 conductive domain, we choose to use an equivalent (\mathbf{A}, V) potential formulation of the
 71 problem, see for instance [31] and references therein. This formulation has the advan-
 72 tage of depending only on the topology of the whole computational domain. In order
 73 to avoid adapting the mesh to different probe positions, we reformulate the problem
 74 in terms of scattered fields and extend the potential formulation to this setting. The
 75 main drawback of (\mathbf{A}, V) formulation is that it increases the size of the discrete sys-
 76 tem as compared to other classical formulations in terms of electric or magnetic fields
 77 [31]. In addition, for ECT, depending on the number of coils and probe positions,
 78 the number of problems to solve can be very large (in the order of thousands) at each
 79 gradient-descent iteration. Using the formulation in terms of scattered fields, we are
 80 then faced with a critical issue encountered in large-scale inverse problems: how to
 81 efficiently solve a large-scale forward problem for a large number of right-hand sides?

82 For large-scale simulations, exact LU factorizations are not tractable using a
 83 direct solver such as MUMPS [2]. Instead, specialized iterative methods may be
 84 used. Indeed, they leverage the fact that the available right-hand sides, yielded by
 85 the different coils and their positions, are available simultaneously. Block Krylov
 86 methods are part of these specialized iterative methods. They have a higher arithmetic
 87 intensity than standard Krylov methods, and typically converge in fewer iterates since
 88 they generate larger Krylov subspaces at each iteration. In practice, these methods
 89 are already used in geophysics [8] or tomography [38], where there are similar needs
 90 for efficient solvers capable of dealing with multiple right-hand sides.

91 We here benchmark four different iterative solvers: GMRES [33], GCRODR [27],
 92 block GMRES [15] and block GCRODR [23]. While GMRES and to a lesser extent
 93 GCRODR are widely used algorithms to solve linear systems, they turned out to be

94 non-effective for our inverse problem as they badly scale with the number of right-
 95 hand sides. Block iterative solvers allow the user to solve blocks of right-hand sides at
 96 the same time and are more adapted. However, they are more memory demanding.
 97 Given the size of the blocks in our problem, handling all right-hand sides (RHS) at
 98 the same time is not tractable. As such, we split the full block of RHS into smaller
 99 sub-blocks and try different sub-block size to determine an optimal parameter for our
 100 application. The difference between block GMRES and block GCRODR lies in the
 101 recycling option provided by the latter: from one block to another, we are able to
 102 recycle basis vectors from one sub-block solve to another. Recycling is supposed to
 103 provide a faster convergence. In our case, while the number of iterates indeed lowers
 104 with block GCRODR, we observed that the solve time increases. We thus propose a
 105 new redistribution scheme to increase the performance of block GCRODR.

106 The effectiveness of the whole inversion procedure is tested for realistic experimen-
 107 tal scenarios and realistic physical parameters provided by our industrial partner. We
 108 simulate measurements associated with so-called SAX probe (axisymmetric probe)
 109 and measurements associated with so-called SMX probe (non-axisymmetric). We
 110 demonstrate in particular the efficiency of our algorithm in handling both scenarios.
 111 Thanks to block Krylov methods, inversion of data provided by SMX probe for a
 112 typical experiment is feasible within a reasonable time.

113 The paper is organized as follows. In [section 2](#), the (\mathbf{A}, V) formulation is presented
 114 and extended to the scattered field. In [section 3](#), the general context of the appli-
 115 cation at hand is explained and the inversion algorithm for reconstructing deposits
 116 is described. Multiple numerical solution strategies are benchmarked in [section 4](#).
 117 The optimal configuration is then used for complete inverse simulations in [section 5](#).
 118 Concluding remarks are given in [section 6](#).

119 2. The direct problem.

120 **2.1. Problem formulation.** Let $\Omega \subset \mathbb{R}^3$ be the computational domain of in-
 121 terest inside the SG that is assumed to be with Lipschitz boundary and later will
 122 be assumed to be also simply connected with connected boundary and either regular
 123 or convex polyhedral. The medium physical parameters, namely the electric permit-
 124 tivity $\varepsilon(\mathbf{x}) > 0$, the conductivity $\sigma(\mathbf{x}) \geq 0$ and the magnetic permeability $\mu(\mathbf{x}) > 0$
 125 are assumed to be piecewise constant functions. Let Ω_C be the conductive domain,
 126 i.e., the region where $\sigma \neq 0$ and $\Omega_I = \Omega \setminus \Omega_C$ be the insulator domain. We denote
 127 $\Gamma := \partial\Omega_I \cap \partial\Omega_C$ the interface between insulator and conductor domains.

128 Let \mathbf{J} be the current density and (\mathbf{E}, \mathbf{H}) be the electromagnetic field induced by
 129 the current. Considering a time-harmonic framework, with ω being the pulsation and
 130 the eddy-current approximation $\omega\varepsilon \ll \sigma$, the 3D time-harmonic Maxwell equations
 131 lead to the following system:

$$132 \quad (2.1) \quad \begin{cases} \mathbf{curl} \mathbf{E} - i\omega\mu\mathbf{H} = \mathbf{0} & \text{in } \Omega, \\ \mathbf{curl} \mathbf{H} - \sigma\mathbf{E} = \mathbf{J} & \text{in } \Omega, \\ \operatorname{div}(\varepsilon\mathbf{E}) = 0 & \text{in } \Omega_I, \end{cases}$$

133 that has to be complemented with some appropriate boundary conditions on $\partial\Omega$ and
 134 some compatibility conditions on $\partial\Omega_I$ for the normal component of $\mathbf{E}|_{\partial\Omega_I}$. The latter
 135 will not be specified since it is not needed in the adopted formulation hereafter. For
 136 the boundary conditions on $\partial\Omega$, we shall impose $\mathbf{H} \times \mathbf{n} = \mathbf{0}$ where \mathbf{n} denotes the
 137 outward normal.

138 Solving [\(2.1\)](#) can be proven to be rather difficult, as the eddy-current approxima-

139 tion introduces a different behavior of the fields in the insulator and in the conductor
 140 domains. For instance, when $\Omega_{\mathcal{I}}$ and/or its boundary are not simply connected the
 141 computation of (\mathbf{E}, \mathbf{H}) may require the introduction of cuts and associated harmonic
 142 functions. For the application described later, the computational domain Ω is simply
 143 connected with connected boundary. Therefore, in order to remove the issue related
 144 to the connectivity of $\Omega_{\mathcal{I}}$, we propose here to formulate (2.1) using the potentials
 145 (\mathbf{A}, V) defined by (see for instance [31]):

$$146 \quad (2.2) \quad \mu \mathbf{H} = \mathbf{curl} \mathbf{A} \text{ in } \Omega, \quad \mathbf{E} = i\omega \mathbf{A} + \nabla V \text{ in } \Omega_C,$$

147 together with the Coulomb gauge $\operatorname{div} \mathbf{A} = 0$ in Ω and the additional the boundary
 148 condition $\mathbf{A} \cdot \mathbf{n} = 0$ on $\partial\Omega$. The existence of the decomposition is motivated by the
 149 first equation in (2.1). Inserting these definitions into the second equation of (2.1)
 150 and the boundary conditions on $\partial\Omega$ yield the following system:

$$151 \quad (2.3) \quad \begin{cases} \mathbf{curl}(\mu^{-1} \mathbf{curl} \mathbf{A}) - \sigma(i\omega \mathbf{A} + \nabla V) = \mathbf{J} & \text{in } \Omega, \\ \operatorname{div} \mathbf{A} = 0 & \text{in } \Omega, \\ \mathbf{A} \cdot \mathbf{n} = 0 \text{ and } (\mu^{-1} \mathbf{curl} \mathbf{A}) \times \mathbf{n} = \mathbf{0} & \text{on } \partial\Omega. \end{cases}$$

152 These equations allow to compute the electromagnetic field inside the conductive
 153 material and would be sufficient to simulate the impedance measurements we are
 154 interested in later.

155 *Remark 2.1.* Note that V is defined up to an additive constant in each connected
 156 component of Ω_C . In fact, since Ω is simply connected with connected boundary, there
 157 exists a function \tilde{V} such that $\mathbf{E} = i\omega \mathbf{A} + \nabla \tilde{V}$ in Ω . The function \tilde{V} may therefore differ
 158 from the function V determined by (2.3) by a constant in each connected component
 159 of Ω_C .

160 In a finite element framework, when solving numerically (2.3), the gauge condition is
 161 difficult to implement as it requires to build a discrete function space of divergence-free
 162 functions. To remove the condition from the functional space, we adopt the procedure
 163 introduced in [9] and modify the first equation in (2.3) as

$$164 \quad \mathbf{curl}(\mu^{-1} \mathbf{curl} \mathbf{A}) - \mu_*^{-1} \nabla(\operatorname{div} \mathbf{A}) - \sigma(i\omega \mathbf{A} + \nabla V) = \mathbf{J} \quad \text{in } \Omega,$$

165 where μ_* is a positive constant. It can be chosen in practice as an average value of
 166 μ . By adding the penalization term, we lose the relation that links \mathbf{E} and \mathbf{J} inside Ω ,
 167 namely $\operatorname{div}(\sigma \mathbf{E}) = -\operatorname{div} \mathbf{J}$ in Ω , that should be added to the system. Assuming that
 168 $\operatorname{div} \mathbf{J} = 0$ in Ω , we then obtain the following equivalent system

$$169 \quad (2.4) \quad \begin{cases} \mathbf{curl}(\mu^{-1} \mathbf{curl} \mathbf{A}) - \mu_*^{-1} \nabla(\operatorname{div} \mathbf{A}) - \sigma(i\omega \mathbf{A} + \nabla V) = \mathbf{J} & \text{in } \Omega, \\ \operatorname{div}(\sigma(i\omega \mathbf{A} + \nabla V)) = 0 & \text{in } \Omega_C, \\ \sigma(i\omega \mathbf{A} + \nabla V) \cdot \mathbf{n} = 0 & \text{on } \Gamma, \\ \mathbf{A} \cdot \mathbf{n} = 0 \text{ and } (\mu^{-1} \mathbf{curl} \mathbf{A}) \times \mathbf{n} = \mathbf{0} & \text{on } \partial\Omega. \end{cases}$$

Let us introduce the function spaces

$$\begin{aligned} \mathbf{H}(\operatorname{curl}, \Omega) &:= \{\mathbf{A} \in L^2(\Omega)^3, \mathbf{curl} \mathbf{A} \in L^2(\Omega)^3\} \\ \mathbf{H}_0(\operatorname{div}, \Omega) &:= \{\mathbf{A} \in L^2(\Omega)^3, \operatorname{div} \mathbf{A} \in L^2(\Omega), \mathbf{A} \cdot \mathbf{n} = 0 \text{ on } \partial\Omega\} \end{aligned}$$

and set $\mathbf{X}(\Omega) := \mathbf{H}(\text{curl}, \Omega) \cap \mathbf{H}_0(\text{div}, \Omega)$. Assume that Ω_C has M connected components Ω_C^i , $i = 1, \dots, M$, then we define

$$\tilde{H}^1(\Omega_C) := \left\{ V \in H^1(\Omega), \int_{\Omega_C^i} V dx = 0, i = 1, \dots, M \right\}.$$

170 Multiplying the first equation, resp. the second equation, in (2.4) with a test function
 171 $\bar{\mathbf{B}} \in \mathbf{X}(\Omega)$, resp. $\bar{Q}/i\omega \in \tilde{H}^1(\Omega_C)$, integrating by parts over Ω , using the boundary
 172 conditions, and summing the resulting equations leads to the following variational
 173 formulation [31, 17]:

$$174 \quad (2.5) \quad \mathcal{A}((\mathbf{A}, V), (\mathbf{B}, Q)) = \mathcal{L}((\mathbf{B}, Q)), \quad \forall (\mathbf{B}, Q) \in \mathbf{X}(\Omega) \times \tilde{H}^1(\Omega_C)$$

$$\begin{aligned} \text{with: } \mathcal{A}((\mathbf{A}, V), (\mathbf{B}, Q)) &:= \int_{\Omega} [\mu^{-1} \mathbf{curl} \mathbf{A} \cdot \mathbf{curl} \bar{\mathbf{B}} + \mu_*^{-1} (\text{div} \mathbf{A})(\text{div} \bar{\mathbf{B}})] dx \\ &+ \frac{1}{i\omega} \int_{\Omega_C} \sigma (i\omega \mathbf{A} + \nabla V) \cdot \overline{(i\omega \mathbf{B} + \nabla Q)} dx, \\ \mathcal{L}((\mathbf{B}, Q)) &:= \int_{\Omega} \mathbf{J} \cdot \bar{\mathbf{B}} dx. \end{aligned}$$

175 We now can state the following theorem that can be deduced from a more general
 176 result in [31, chapter 6], see also [17].

177 **THEOREM 2.2.** *Assume that Ω is simply connected with connected boundary and*
 178 *that $\mathbf{J} \in X(\Omega)'$. Then problem (2.5) admits a unique solution $(\mathbf{A}, V) \in \mathbf{X}(\Omega) \times$*
 179 *$\tilde{H}^1(\Omega_C)$. Assume in addition that $\text{div} \mathbf{J} = 0$ in Ω . Then the solution of (2.5) satisfies*
 180 *(2.4) or equivalently (2.3) and the fields (\mathbf{E}, \mathbf{H}) defined by (2.2) verify the first two*
 181 *equations in (2.1).*

182 **2.2. Scattered field formulation.** As explained later, the goal will be to re-
 183 construct a deposit that appears in a reference configuration characterized by physical
 184 parameters σ_0 and μ_0 , and associated conductive part Ω_C^0 . Let us denote by $(\mathbf{E}^0, \mathbf{H}^0)$
 185 the electromagnetic field associated with this configuration and a source term \mathbf{J} . This
 186 field verifies in particular

$$187 \quad (2.6) \quad \begin{cases} \mathbf{curl} \mathbf{E}^0 - i\omega \mu_0 \mathbf{H}^0 = \mathbf{0} & \text{in } \Omega, \\ \mathbf{curl} \mathbf{H}^0 - \sigma_0 \mathbf{E}^0 = \mathbf{J} & \text{in } \Omega, \\ \mathbf{H}^0 \times \mathbf{n} = \mathbf{0} & \text{on } \partial\Omega. \end{cases}$$

In order to speed up calculations in cases where a large number of different source terms \mathbf{J} is used and avoid remeshing (see the discussion at the end of this section), it is more advantageous to solve for the scattered fields

$$(\mathbf{E}^s, \mathbf{H}^s) := (\mathbf{E}, \mathbf{H}) - (\mathbf{E}^0, \mathbf{H}^0)$$

188 assuming that $(\mathbf{E}^0, \mathbf{H}^0)$ has been computed offline. As above, one can set up equations
 189 for the scattering field in terms of potentials. We hereafter give an outline. Taking
 190 the difference between the two first equations of (2.1) and (2.6) we obtain

$$191 \quad (2.7) \quad \mathbf{curl} \mathbf{E}^s - i\omega(\mu \mathbf{H} - \mu_0 \mathbf{H}^0) = \mathbf{0} \quad \text{in } \Omega.$$

192 As previously, when Ω is simply connected with connected boundary, this equation
193 implies the existence of potentials (\mathbf{A}^s, V^s) such that

$$194 \quad (2.8) \quad \mu \mathbf{H} - \mu_0 \mathbf{H}^0 = \mathbf{curl} \mathbf{A}^s \text{ in } \Omega, \quad \mathbf{E}^s = i\omega \mathbf{A}^s + \nabla V^s \text{ in } \Omega_C,$$

195 with the Coulomb gauge $\text{div} \mathbf{A}^s = 0$ in Ω and the additional boundary condition
196 $\mathbf{A}^s \cdot \mathbf{n} = 0$ on $\partial\Omega$. Inserting these definitions into the second equation of (2.1) and
197 the boundary conditions on $\partial\Omega$ yield the following system:

$$198 \quad (2.9) \quad \begin{cases} \mathbf{curl}(\mu^{-1} \mathbf{curl} \mathbf{A}^s) - \sigma(i\omega \mathbf{A}^s + \nabla V^s + \mathbf{E}^0) = \mathbf{J}_0 & \text{in } \Omega, \\ \text{div} \mathbf{A}^s = 0 & \text{in } \Omega, \\ \mathbf{A}^s \cdot \mathbf{n} = 0 \text{ and } (\mu^{-1} \mathbf{curl} \mathbf{A}^s) \times \mathbf{n} = \mathbf{0} & \text{on } \partial\Omega, \end{cases}$$

with \mathbf{J}_0 defined by

$$\mathbf{J}_0 := \mathbf{curl} \left(\left(1 - \frac{\mu_0}{\mu} \right) \mathbf{H}^0 \right) - \sigma_0 \mathbf{E}^0 \quad \text{in } \Omega.$$

199 Clearly, if $\text{div} \mathbf{J} = 0$ in Ω , then we also have $\text{div} \mathbf{J}_0 = 0$ in Ω and therefore as explained
200 previously, the system (2.9) can be equivalently written as

$$201 \quad (2.10) \quad \begin{cases} \mathbf{curl}(\mu^{-1} \mathbf{curl} \mathbf{A}^s) - \mu_*^{-1} \nabla(\text{div} \mathbf{A}^s) - \sigma(i\omega \mathbf{A}^s + \nabla V^s + \mathbf{E}^0) = \mathbf{J}_0 & \text{in } \Omega, \\ \text{div}(\sigma(i\omega \mathbf{A}^s + \nabla V^s + \mathbf{E}^0)) = 0 & \text{in } \Omega_C, \\ \sigma(i\omega \mathbf{A}^s + \nabla V^s + \mathbf{E}^0) \cdot \mathbf{n} = 0 & \text{on } \Gamma, \\ \mathbf{A}^s \cdot \mathbf{n} = 0 \text{ and } (\mu^{-1} \mathbf{curl} \mathbf{A}^s) \times \mathbf{n} = \mathbf{0} & \text{on } \partial\Omega. \end{cases}$$

202 Similarly to (2.5), the variational formulation of this problem can be written as

$$203 \quad (2.11) \quad \mathcal{A}((\mathbf{A}^s, V^s), (\mathbf{B}, Q)) = \mathcal{L}^s((\mathbf{B}, Q)), \quad \forall (\mathbf{B}, Q) \in \mathbf{X}(\Omega) \times \tilde{H}^1(\Omega_C)$$

where the right-hand side can be expressed as

$$\mathcal{L}^s((\mathbf{B}, Q)) := \int_{\Omega} \left(1 - \frac{\mu_0}{\mu} \right) \mathbf{H}^0 \cdot \mathbf{curl} \bar{\mathbf{B}} \, dx - \frac{1}{i\omega} \int_{\Omega_C} (\sigma - \sigma_0) \mathbf{E}^0 \cdot \overline{(i\omega \mathbf{B} + \nabla Q)} \, dx.$$

204 We can state the following theorem on the well-posedness of this problem and the
205 equivalence with the original problem.

206 **THEOREM 2.3.** *Assume that Ω is simply connected with connected boundary and*
207 *that $(\mathbf{E}^0, \mathbf{H}^0) \in L^2(\Omega)^3 \times L^2(\Omega)^3$. Then, problem (2.5) admits a unique solution*
208 *$(\mathbf{A}^s, V^s) \in \mathbf{X}(\Omega) \times \tilde{H}^1(\Omega_C)$. Assume in addition that $(\mathbf{E}^0, \mathbf{H}^0)$ satisfies (2.6) with*
209 *$\text{div} \mathbf{J} = 0$ in Ω . Then, the solution of (2.11) satisfies (2.10) or equivalently (2.9) and*
210 *the fields (\mathbf{E}, \mathbf{H}) defined by (2.8) verify the first two equations in (2.6).*

211 In the context of deposit detection presented below, the probe takes measures at reg-
212 ular positions alongside the tube. A typical scan requires up to 140 probe positions:
213 for each position, a new computation of the electromagnetic field is required. Consid-
214 ering the variational formulation (2.5), as the right-hand side depends on the current
215 density \mathbf{J} located in the probe, computation of the field for each position requires
216 a different mesh where the probe is at the proper position. Conversely, in (2.11),
217 the right-side depends on the incident field only on the domain where $\sigma \neq \sigma_0$ or
218 $\mu \neq \mu_0$, which is independent from the probe position. Consequently, assuming that
219 the incident fields are computed offline for any probe position, solving (2.11) do not
220 require remeshing for different probe positions and therefore is more computationally
221 efficient.

222 **2.3. Finite element discretization.** To solve (2.5) or (2.11), we shall use
 223 finite elements on a tetrahedralization \mathcal{T}_h of the domain Ω , where h is the mesh
 224 size. A tetrahedralization of the conductive domain would be a restriction of \mathcal{T}_h
 225 to Ω_C . Let K indicate an element of the tetrahedralization. We choose piece-
 226 wise affine Lagrange elements to discretize the scalar potential V . We denote by
 227 $V_h^1(\Omega_C) := \{v_h \in C^0(\Omega_C) / \forall K \subset \mathcal{T}_h, v_h|_K \in \mathbb{P}^1(K)\}$ the discrete space associated
 228 with $H^1(\Omega_C)$.

229 Assuming that Ω is a regular domain, the space $\mathbf{H}(\text{curl}, \Omega) \cap \mathbf{H}_0(\text{div}, \Omega)$ is iso-
 230 metric to $H^1(\Omega)^3 \cap \mathbf{H}_0(\text{div}, \Omega)$. This is also the case when Ω is a convex cylinder or
 231 polyhedron [9], which is the case of our numerical experiments. In this case, piecewise
 232 affine Lagrange elements can also be used to discretize each component of the vector
 233 potential. The discrete space associated with $X(\Omega)$ is then

$$234 \quad \mathbf{X}_h^1(\Omega) = \{\mathbf{w}_h \in (C^0(\Omega))^3 / \mathbf{w}_h|_K \in (\mathbb{P}^1(K))^3 \forall K \in \mathcal{T}_h, \mathbf{w}_h \cdot \mathbf{n} = 0 \text{ on } \partial\Omega\}.$$

Since the scalar potential is assumed to have zero mean value in each connected
 component of Ω_C , we enforce this condition by adding a penalization of the form
 $\int_{\Omega_C} \delta_0 \sigma V \bar{Q} \, dx$ where $0 < \delta_0 \ll 1$. The value of δ_0 is chosen empirically using cali-
 bration on a test case. To summarize, the discrete system is built by replacing the
 sesquilinear form \mathcal{A} by

$$\mathcal{A}((\mathbf{A}, V), (\mathbf{B}, Q)) + \frac{1}{i\omega} \int_{\Omega_C} \delta_0 \sigma V \bar{Q} \, dx,$$

235 and replacing the variational space $X(\Omega) \times \tilde{H}^1(\Omega)$ with $\mathbf{X}_h^1(\Omega) \times V_h^1(\Omega_C)$. The numer-
 236 ical implementation of the resulting scheme has been done using the finite element
 237 library FreeFEM [18].

238 3. The inverse problem.

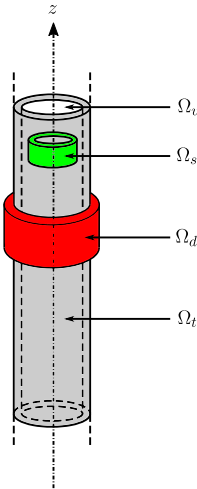


Fig. 1: Domain Ω for the Maxwell equations

239 **3.1. Description of the experiment.** Let us specify the composition of the
 240 computational domain in the context of shape reconstruction inside a SG [26]. Con-

241 sider a U-shaped tube, the focus being placed here on the straight part of the tube
 242 which is assumed to be a cylinder around the z -axis. We denote by:

- 243 • Ω_v the vacuum domain inside and outside the tube, with physical parameters
 244 $(\sigma_v = 0, \mu_v)$;
- 245 • Ω_t the domain occupied by the tube made out of conductive material, with
 246 physical parameters (σ_t, μ_t) ;
- 247 • Ω_d the deposit domain located in the exterior of the tube, with physical
 248 parameters (σ_d, μ_d) ;
- 249 • Ω_s the domain occupied by the probe placed inside the tube.

250 The current density \mathbf{J} is considered to be compactly supported in Ω_s and divergence-
 251 free. **Figure 1** displays the main features of the domain. We assume here that the
 252 probe conductivity can be neglected compared to the remaining conductive materials.
 253 The conducting part Ω_C is then made of the tube and the deposit. The insulating
 254 part is made of the vacuum and the probe. The computational domain Ω is a cylinder
 255 of height H and radius R chosen to be sufficiently large.

The physical parameters are assumed to be known a priori and the only unknown
 for the inverse problem is the domain Ω_d . In this context and referring to the notation
 of the previous section, the reference media is defined by (with χ_O denoting the
 characteristic function of a domain O),

$$\sigma_0 := \sigma_t \chi_{\Omega_t} \quad \mu_0 := \mu_t \chi_{\Omega_t} + \mu_v \chi_{\Omega_v} + \mu_s \chi_{\Omega_s}$$

while

$$\sigma := \sigma_t \chi_{\Omega_t} + \sigma_d \chi_{\Omega_d} \quad \mu := \mu_t \chi_{\Omega_t} + \mu_v \chi_{\Omega_v} + \mu_s \chi_{\Omega_s} + (\mu_d - \mu_v) \chi_{\Omega_d}.$$

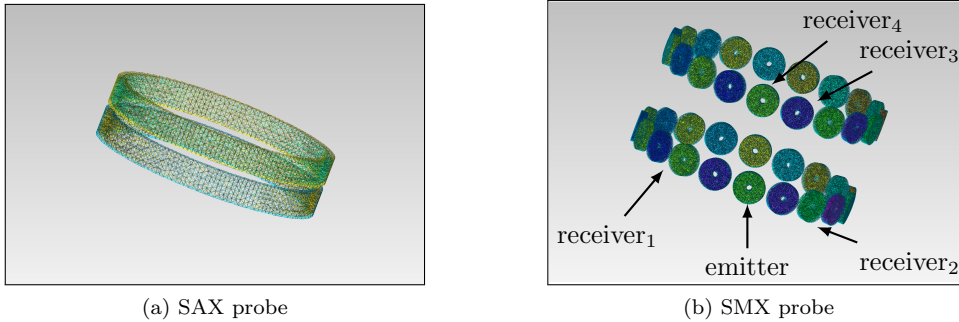


Fig. 2: Two probes used for ECT

256 The data for the deposit identification is collected as follows. A probe composed
 257 of N_c coils is inserted inside the tube to one end. The probe is then pulled at constant
 258 speed to the other end. At regular positions, the coils are subjected to a current I ,
 259 inducing an electromagnetic wave. **Figure 2** displays two examples of probes used
 260 in ECT: while the SAX probe is composed of two coaxial coils, the SMX probe
 261 has two rows of coils placed around the probe axis. Note that due to its structure,
 262 the former provides information that is averaged on the azimuthal component. We
 263 denote by N_p the number of probe positions. The coil l used to generate the fields
 264 is called the emitter, while the coil k measuring the flow is called the receiver. The

265 corresponding measured signal, called impedance signal and denoted ΔZ_{kl} , has the
 266 following expression [24]:

$$267 \quad (3.1) \quad \Delta Z_{kl} = \frac{1}{i\omega I^2} \int_{\Omega_d} \left(\left(\frac{1}{\mu} - \frac{1}{\mu_0} \right) (\mathbf{curl} \mathbf{E}_k) \cdot (\mathbf{curl} \mathbf{E}_l^0) - i\omega(\sigma - \sigma_0) \mathbf{E}_k \cdot \mathbf{E}_l^0 \right) d\mathbf{x},$$

268 where the notation $(\mathbf{E}_k, \mathbf{H}_k)$ and $(\mathbf{E}_k^0, \mathbf{H}_k^0)$ respectively refers to the solution of (2.1)
 269 and (2.6) where the source term \mathbf{J} is supported by the coil k . Note that from this
 270 definition, we have the equality $\Delta Z_{kl} = \Delta Z_{lk}$ for any k and l .

271

272 In practice, the probes cannot measure ΔZ_{kl} , but rather linear combinations of
 273 these quantities called modes. Consider two coils k (receiver) and l (emitter), then
 274 there are two main modes for these coils:

275 **differential mode** $Z_F = 0.5i(\Delta Z_{ll} - \Delta Z_{kk})$;

276 **absolute mode** $Z_{FA} = 0.5i(\Delta Z_{ll} + \Delta Z_{kk})$.

277 Experimental observations show that each of these modes has different sensitivities
 278 with respect to the deposit. Roughly speaking, Z_F detects better sharp variations
 279 in the shape geometry while Z_{FA} is more suited to identify smooth variations. To
 280 illustrate these observations, Figure 3 displays examples of impedance signals for an
 281 annular deposit between $z_- = -0.5$ cm and $z_+ = 0.05$ cm, at frequency 100 kHz, with
 282 the SAX probe. We do not elaborate here on the specifics of the acquisitions and
 283 refer to [26] for more details.

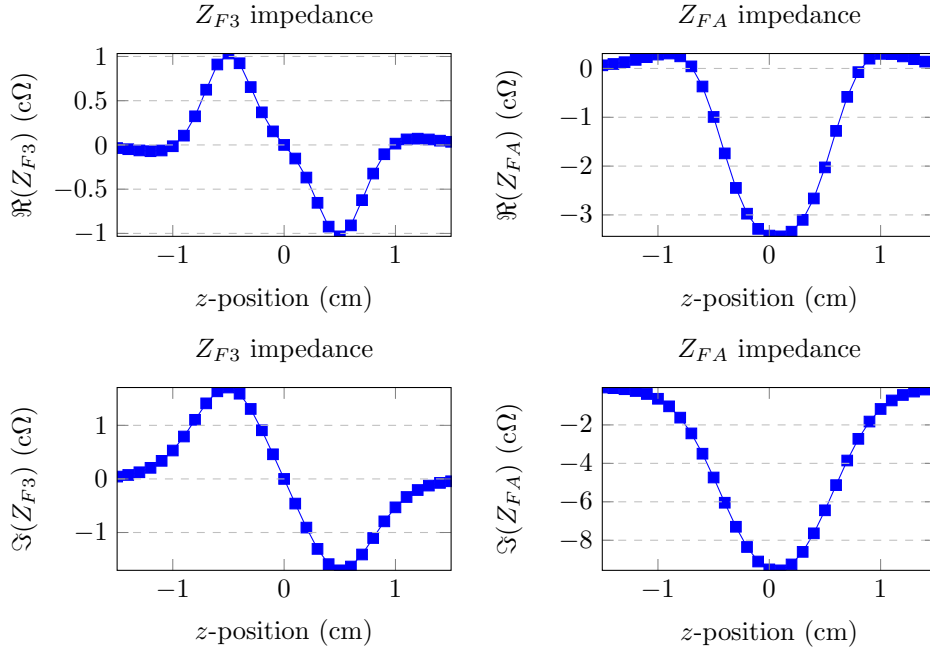


Fig. 3: Example of SAX impedance signals for an annular deposit between $z_- = -0.5$ cm and $z_+ = 0.05$ cm, at frequency 100 kHz (real and imaginary parts on rows and Z_{F3} and Z_{FA} on columns).

284 In practice, the SAX probe can work with three different pulsations $\omega_1 > \omega_2 > \omega_3$
 285 and generates a differential mode for each pulsation. For the lowest pulsation, it

286 generates an additional absolute mode. The conductivity of the tube absorbs most
 287 of the energy delivered by the coil and this absorption increases with the frequency.
 288 This is why we focus here only on $\omega_3 = 2\pi \cdot 10^5 \text{ rad} \cdot \text{s}^{-1}$ as it ensures that some of
 289 the electromagnetic energy reaches the outer part of the tube. As such, a SAX probe
 290 provides two impedance values for each z -position.

291 The SMX probe can also operate at a fourth pulsation $\omega_4 < \omega_3$, though we con-
 292 sider here only ω_3 . It generates absolute mode according to the following acquisition
 293 rule: the emitter coils are contained on the lower row. For each emitter, there are
 294 four associated receiver coils, as displayed in [Figure 2b](#). Since the probe has 19 coils
 295 on each row, the device provides 76 impedance values for each z -position.

296 **3.2. Description of the inversion algorithm.** We here give a description of
 297 the adopted inversion strategy to reconstruct the shape and position of deposits from
 298 measured signals. For a given z -position of the probe, let us denote by $\mathbf{Z}_{\text{meas}}^i(z)$
 299 the measured signal and $\mathbf{Z}^i(\Omega_d, z)$ the computed signal for a given shape Ω_d , where
 300 $i = 1, \dots, N_s$ refer to the index of the signals ($N_s = 2$ for SAX and $N_s = 76$ for SMX).
 301 The numerical evaluation of the impedance signal is obtained by solving [\(2.11\)](#). We
 302 now formulate the inverse problem as an optimization problem for a least squares
 303 misfit cost functional:

$$304 \quad \min_{\Omega_d} \left(\mathcal{J}(\Omega_d) = \frac{1}{N_s} \sum_{i=0}^{N_s} \int_{z_-}^{z_+} |\mathbf{Z}^i(\Omega_d, \zeta) - \mathbf{Z}_{\text{meas}}^i(\zeta)|^2 d\zeta \right).$$

306 This formulation has been solved [\[21, 17, 30\]](#) using a gradient-descent method and a
 307 boundary variation technique. One drawback of such an approach is that it modifies
 308 at each iteration the computational mesh by moving the shape boundary accordingly,
 309 imposing a remeshing step. A possible remedy has been proposed in [\[30\]](#) by the
 310 use of a fixed Cartesian mesh in the region containing the deposit and consider only
 311 boundaries that can be exactly represented by the considered mesh. Indeed, such a
 312 procedure imposes a strong bias on the reconstruction and cannot handle complex
 313 topologies. We propose here to use a level-set approach [\[25\]](#) where the boundary $\partial\Omega_d$
 314 is implicitly encoded by the zero level-set of a function ψ . Denote by $D \subset \Omega$ a domain
 315 containing all admissible shapes Ω_d , called region of interest (ROI). The function ψ
 316 is then defined on D and verifies

$$317 \quad \psi(\mathbf{x}) \begin{cases} < 0 & \text{if } \mathbf{x} \in \Omega_d, \\ = 0 & \text{if } \mathbf{x} \in \partial\Omega_d, \\ > 0 & \text{if } \mathbf{x} \in D/\overline{\Omega_d}. \end{cases}$$

318 Since it is not directly correlated to the solution of the forward problem, the domain
 319 D is meshed independently from the mesh used for computing the solutions to [\(2.11\)](#).
 320 However, the two meshes are kept fixed during iterations. The following scheme then
 321 requires only interpolation operations from one to another.

322 Following previous works on level-set-based shape optimization [\[1, 10\]](#), under this
 323 model, the shape update at each iteration is equivalent to convection of the level-set
 324 according to the Hamilton–Jacobi equation:

$$325 \quad (3.2) \quad \frac{\partial\psi}{\partial t} + G|\nabla\psi| = 0 \quad \text{in } D,$$

326 where G is a deformation direction defined on D as an extension of the shape gradient
 327 of the cost functional \mathcal{J} as explained below. Note that the convection time is a step

328 that needs to be adjusted at each iteration in order to ensure a fast convergence. In
 329 our numerical algorithm, (3.2) is solved using a backward method of characteristics
 330 as proposed in [6].

331 *Evaluation of the descent direction G :* The computation of the descent direc-
 332 tion uses the solution of an additional variational problem for so-called adjoint state.
 333 Following [21, 30], it is defined as the field $(\mathbf{P}, W) \in X(D) \times \tilde{H}^1(\Omega_C)$, solution of:

(3.3)

$$334 \quad \mathcal{A}^*((\mathbf{P}, W), (\mathbf{B}, Q)) = \overline{\mathcal{A}((\mathbf{B}, Q), (\mathbf{P}, W))} = \mathcal{L}^*((\mathbf{B}, Q)), \forall (\mathbf{B}, Q) \in \mathbf{X}(\Omega) \times \tilde{H}^1(\Omega_C),$$

335

$$336 \quad \text{with } \mathcal{L}^*((\mathbf{B}, Q)) := \int_{\Omega_d} \left(\frac{-1}{i\omega} \left(\frac{1}{\mu} - \frac{1}{\mu_0} \right) \mathbf{curl} \bar{\mathbf{B}} \cdot \mathbf{curl} \bar{\mathbf{E}}^0 \right. \\ \left. + \frac{1}{i\omega} (\sigma - \sigma_0) \overline{(i\omega \mathbf{B} + \nabla Q)} \cdot \bar{\mathbf{E}}^0 \right) dx.$$

337

338

339 These fields can be seen as the Lagrange multiplier of the optimization problem
 340 where the constraint is the variational formulation (2.5). Using these fields, we are
 341 able to write the shape derivative of the cost function as (see [21] for more details on
 342 the calculations):

$$343 \quad \mathcal{J}'(\Omega_d)(\boldsymbol{\theta}) = -\frac{1}{N_s} \sum_{i=1}^{N_s} \frac{\omega}{I^2} \int_{\partial\Omega_d} (\boldsymbol{\theta} \cdot \mathbf{n}) g^i ds.$$

344 For a signal i , let us denote by k_i (resp. l_i) the index of the receiver (resp. emitter)
 345 coil. The vector $\mathbf{g} = (g^1, \dots, g^{N_s})$ of gradients is then defined by:

$$346 \quad g^i = \begin{cases} g_{l_i l_i} - g_{k_i k_i} & \text{differential mode} \\ g_{l_i l_i} + g_{k_i l_i} & \text{absolute mode,} \end{cases}$$

347 where, for a given emitter coil l and receiver coil k ,

(3.4)

$$348 \quad g_{kl} := \int_{z_{\min}}^{z_{\max}} \Re \left(\overline{(Z(\Omega_d, \zeta) - Z_{\text{meas}}(\zeta))} \left\{ \left[\frac{1}{\mu} \right] (\mathbf{n} \cdot \mathbf{curl} \mathbf{A}_k) (\mathbf{n} \cdot \mathbf{curl} \bar{\mathbf{P}}_1 - \mathbf{n} \cdot \mathbf{curl} \mathbf{A}_l^0) \right. \right. \\ \left. \left. - [\mu] \left(\frac{1}{\mu} (\mathbf{curl} \mathbf{A}_k) \times \mathbf{n} \right) \cdot \left(\frac{1}{\mu_0} (\mathbf{curl} (\bar{\mathbf{P}}_1)_+) \times \mathbf{n} - \frac{1}{\mu_0} (\mathbf{curl} \mathbf{A}_l^0) \times \mathbf{n} \right) \right. \right. \\ \left. \left. + \frac{[\sigma]}{i\omega} (i\omega (\mathbf{A}_k)_\tau + \nabla_\tau V_k) \cdot \overline{(i\omega (\mathbf{P}_l)_\tau + \nabla_\tau W_l + (\mathbf{E}_l^0)_\tau)} \right\} \Big|_{\zeta} \right) d\zeta.$$

349 The notation \mathbf{A}_ζ refers to the solution of the direct problem with the source term
 350 generated by the coils at position ζ . For a vector field \mathbf{a} , $\mathbf{a}_\tau = \mathbf{a} - (\mathbf{a} \cdot \mathbf{n})\mathbf{n}$ denotes the
 351 tangential part of \mathbf{a} on a surface Γ with normal vector \mathbf{n} . $\nabla_\tau V$ denotes the tangential
 352 part of ∇V .

353 If one chooses a descent $\boldsymbol{\theta}$ such that,

$$354 \quad (3.5) \quad \boldsymbol{\theta} = \gamma \frac{1}{N_s} \sum_{i=1}^{N_s} g^i \mathbf{n} \quad \text{on } \partial\Omega_d,$$

355 where γ is a positive constant sufficiently small, then $\boldsymbol{\theta}$ is a descent direction for \mathcal{J} .
 356 Note that under a level-set approach, the role of γ is replaced by the length Δt of the
 357 time interval that we use to convect ψ between two iterations using (3.2), see Figure 4.
 358

359 In order to solve the convection problem (3.2), from an initial state defined by
 360 ψ_0 (where ψ_0 is a level-set encoding $\partial\Omega_d$), the deformation direction G needs to be
 361 specified for any point in D . We first define a $H^1(D)$ shape gradient associated with
 362 \mathcal{J} by considering $\mathbf{G} \in H^1(D)^3$, solution of, $\forall \boldsymbol{\theta} \in H^1(D)^3$,

$$363 \quad (3.6) \quad \int_D \left(\sum_{i=1}^3 \alpha \nabla \mathbf{G}_i \cdot \nabla \boldsymbol{\theta}_i + \mathbf{G}_i \boldsymbol{\theta}_i \right) dx = -\mathcal{J}'(\Omega_d)(\boldsymbol{\theta}) = \frac{1}{N_s} \sum_{i=1}^{N_s} \frac{\omega}{I^2} \int_{\partial\Omega_d} (\boldsymbol{\theta} \cdot \mathbf{n}) g^i ds$$

where $\alpha > 0$ is chosen empirically and can be seen as a regularization parameter for
 the descent direction. Obviously, taking $\boldsymbol{\theta} = \mathbf{G}$ provides a descent direction for \mathcal{J} .
 We then set $G = |\mathbf{G}|$ in D . The right-hand side of (3.6) requires in principle explicit
 identification of $\partial\Omega_d$ which we would like to avoid during iterations. This is done by
 observing that

$$\int_{\partial\Omega_d} (\boldsymbol{\theta} \cdot \mathbf{n}) g^i ds = \frac{1}{2} \int_D \nabla(\text{sgn}(\psi_0)) \cdot \boldsymbol{\theta} g^i dx \quad \forall \boldsymbol{\theta} \in H^1(D)^3,$$

364 where the right-hand side is to be understood as a duality product and $\text{sgn}(\psi_0) :=$
 365 $\psi_0/|\psi_0|$. The resulting complete inversion algorithm is summarized in Figure 4.

```

1: input:  $N_p \times N_c$  impedance measurements on a  $z$  interval
2:   incident fields ( $\mathbf{E}^0$ ), for each coil at each probe position
3: initialize  $\psi = \psi_0$ , the gradient speed  $G$  and choose  $\Delta t$  and  $\alpha$ 
4: while  $\mathcal{J} > \eta$  do
5:    $\mathcal{J}_0 = \mathcal{J}$ 
6:   compute the gradient  $\mathbf{G}$  on  $D$ 
7:   convect level-set  $\psi$  for a time interval  $\Delta t$  and a deformation speed  $G$ 
8:   use  $\psi(\Delta t)$  to encode the functions  $\sigma$  and  $\mu$ 
9:   solve the direct problem for each probe position and coil
10:  compute  $\mathcal{J}$ 
11:  if  $\mathcal{J} < \mathcal{J}_0$  then
12:    solve the adjoint problem for each probe position and coil
13:    compute gradient  $\mathbf{g}$  for each signal
14:     $\psi_0 = \psi(\Delta t)$ 
15:  else
16:    decrease time-step  $\Delta t = \Delta t/2$ 
17:  end if
18: end while

```

Fig. 4: Reconstruction algorithm

366 As indicated in Figure 4, for one loop iteration, the number of finite element
 367 problems to solve is $p = N_p \times N_c$ (resp. $N_p \times N_c/2$) for the direct (resp. adjoint)
 368 problem. For the adjoint problem, problems are solved only for the emitters. We
 369 denote by n the number of degrees of freedom of the problem: $n = n_A + n_V$, with n_A
 370 (resp. n_V) the number of degrees of freedom for \mathbf{A}^s (resp. V^s).

371 Let us consider the direct problem. Using the scattered field formulation (2.11),
 372 from one problem to another, the sesquilinear form \mathcal{A} remains the same. Only the
 373 right-hand side changes. Solving for all probe positions is equivalent to solving a block
 374 system of the form:

$$375 \quad (3.7) \quad \begin{pmatrix} \mathbb{M}_{AA} & \mathbb{M}_{AV} \\ \mathbb{M}_{VA} & \mathbb{M}_{VV} \end{pmatrix} \begin{pmatrix} \mathbf{X}_A \\ \mathbf{X}_V \end{pmatrix} = \begin{pmatrix} \mathbf{B}_A \\ \mathbf{B}_V \end{pmatrix},$$

376 where $\mathbb{M}_{AA} \in \mathcal{M}_{n_A, n_A}(\mathbb{C})$, $\mathbb{M}_{AV} \in \mathcal{M}_{n_A, n_V}(\mathbb{C})$, $\mathbb{M}_{VA} \in \mathcal{M}_{n_V, n_A}(\mathbb{C})$, $\mathbb{M}_{VV} \in$
 377 $\mathcal{M}_{n_V, n_V}(\mathbb{C})$, \mathbf{X}_A and $\mathbf{B}_A \in \mathcal{M}_{n_A, p}(\mathbb{C})$, and \mathbf{X}_V and $\mathbf{B}_V \in \mathcal{M}_{n_V, p}(\mathbb{C})$.
 378

379 Depending on the nature of the probe and the length of the tube scanning, the
 380 number of RHS p can greatly increase. With the SAX probe containing two coils,
 381 the number of RHS may remain fairly low. However, using it in ECT may prove
 382 to be inefficient to reconstruct deposit as it averages the configuration around the
 383 azimuthal angle. The best strategy would be to use the SMX probe. As a standard
 384 probe contains 38 coils, the number of RHS increases quite rapidly. Considering that
 385 a typical scan may span up to 140 positions, p is expected to exceed 1,000.

386 Note that measures can be taken to reduce the RHS block size for the SMX probe.
 387 Indeed, as explained before, to generate all signals, one needs to compute the elec-
 388 tromagnetic potentials for each coil at each probe position, cf. the definition of ΔZ_{kl}
 389 in (3.1). However, unlike the SAX probe, the SMX generates only absolute modes.
 390 Thus, by using the equality $\Delta Z_{kl} = \Delta Z_{lk}$ for any coil numbers k and l , we are able
 391 bring down the size of the RHS block from $N_c \times N_p$ to $N_c/2 \times N_p$ as we only need
 392 the direct fields of the emitters, that is to say the lower row.
 393

394 The choice to implicitly define the deposit shape Ω_d with a level-set function ψ
 395 impose to use a fine mesh in the region containing Ω_d . Furthermore, for the potential
 396 formulation, one has four unknowns for each mesh node inside the conductor region.
 397 As a result, the total number of degrees of freedom may exceed one million in a
 398 typical configuration for the direct problem. These constraints combined with the
 399 high number of RHS motivate the investigation of efficient solution strategies. Being
 400 able to tackle this task efficiently is critical as it directly impacts the performance of
 401 the reconstruction algorithm as a whole.

402 **4. Efficient solution strategies.** It was shown in the previous section that
 403 most of the computational burden of the reconstruction algorithm 4 is the successive
 404 solutions of linear systems with large number of right-hand sides, see lines 9 and 12.
 405 Given the size of the discrete problem, exact LU factorizations are not tractable. We
 406 therefore use iterative solvers. The main issue is how to efficiently handle a large number
 407 or RHS. It will be shown in particular that block Krylov methods can efficiently
 408 fix this difficulty. We also propose some adaptations that significantly speedup the
 409 proposed reconstruction algorithm from section 3. Since this step is the most critical
 410 in our inversion algorithm and may apply to other large-scale inverse problems, more
 411 technical details will be provided on some practical implementations.

412 **4.1. Problem formulation.** For simplicity, the notations from (3.7) are cast
 413 into the following condensed form:

$$414 \quad (4.1) \quad \mathbf{AX} = \mathbf{B},$$

415 with $A \in \mathcal{M}_{n,n}(\mathbb{C})$, and both \mathbf{X} and $\mathbf{B} \in \mathcal{M}_{n,p}(\mathbb{C})$. This is done using PETSc [3,
 416 4], the linear algebra backend used in our numerical tests, which can convert the
 417 coefficient matrix from (3.7) stored using a MatNest, into the more general matrix
 418 format MatAIJ. As it is common with high-dimensional problems, a first step for
 419 setting up an efficient solver is the definition of a preconditioner. This preconditioner
 420 must also be able to deal with multiple right-hand sides efficiently. A commonly
 421 used method in this context is the restricted additive Schwarz method [7] (RAS) as
 422 implemented in PETSc. In a distributed-memory parallel context, given a number of
 423 processes N , this preconditioner may be written algebraically as:

$$424 \quad (4.2) \quad M^{-1} = \sum_{i=1}^N \tilde{R}_i^T (R_i A R_i^T)^{-1} R_i,$$

425 where $\{R_i\}_{i=1}^N$ are restriction operators from a global to local vectors on each sub-
 426 domain (or process), possibly with some overlap. $\{\tilde{R}_i\}_{i=1}^N$ are similar operators for
 427 which coefficients on the overlap are set to 0 instead. Readers interested in do-
 428 main decomposition methods are referred to one of the many available monographs
 429 on this matter [35, 37, 11]. An appealing feature of domain decomposition meth-
 430 ods is that the action of local subdomain solvers $\{(R_i A R_i^T)^{-1}\}_{i=1}^N$ are usually com-
 431 puted using exact factorizations with libraries such as MUMPS or MKL PARDISO.
 432 These libraries provide optimized routines for forward eliminations and backward
 433 substitutions on blocks of multiple vectors. Thus, they are good candidates for
 434 our solver which has to deal with thousands of right-hand sides. To conclude this
 435 section, the command line options provided next can be used to setup a PETSc
 436 preconditioner as defined mathematically above: `-pc_type asm -sub_pc_type lu`
 437 `-sub_pc_factor_mat_solver_type mkl_pardiso`. The following results were obtained
 438 on Irène, a system composed of 1,656 nodes with two 24-core Intel Xeon Platinum
 439 8168 clocked at 2.7 GHz.

440 **4.2. Benchmark of available strategies.** PETSc, through its KSPHPDDM
 441 [22] interface to HPDDM [23], implements multiple block Krylov methods. In partic-
 442 ular, the following methods will be considered:

- 443 • standard GMRES [33];
- 444 • standard GCRODR [27];
- 445 • pseudo-block GMRES;
- 446 • pseudo-block GCRODR;
- 447 • block GMRES [15];
- 448 • block GCRODR recalled Figure 7 in order to keep the paper self-contained.

449 Here, standard means that the method is not able to deal with multiple right-hand
 450 sides available simultaneously. Pseudo-block means that the method is mathemati-
 451 cally equivalent to the standard one, in the sense that it generates the same Krylov
 452 subspace, but it fuses similar operations together, e.g., multiple simultaneous sparse
 453 matrix–vector multiplications become a single sparse matrix–dense matrix multipli-
 454 cation. As said in the introduction paragraph of this section, block Krylov methods
 455 generate different subspaces than their standard counterpart. Throughout this sec-
 456 tion, the relative convergence tolerance is set to 10^{-3} and the overlapping Schwarz
 457 preconditioner defined in subsection 4.1 is applied on the right. A restart parameter
 458 of size 40 is used for standard and pseudo-block methods, and it is set to 30 for block
 459 methods, which require more memory.

460 For standard GMRES and GCRODR, instead of solving the full system (4.1), we
 461 consider only the first column of \mathbf{B} and \mathbf{X} . Results for the complete block of p columns

462 may be extrapolated by multiplying the timings obtained by p , since it is expected that
 463 the number of GMRES and GCRODR iterations will be similar as \mathbf{B} is traversed col-
 464 umn by column. These standard solvers could solve the full system, but as highlighted
 465 next, they are extremely inefficient so it would only be a waste of resources. Indeed,
 466 for only the first column of \mathbf{B} , GMRES (resp. GCRODR) converges in 197 (resp. 125)
 467 iterations. This shows an advantage of such a recycling Krylov method, which also
 468 translates to runtime: 8.6 sec against 6.3 sec. However, these timings are not satisfac-
 469 tory, since by extrapolation, it would approximately take 1.8 h (resp. 1.4 h) to solve the
 470 full system with $p = 779$ right-hand sides. The command line options provided next
 471 can be used to setup a PETSc Krylov method as described above: `-ksp_rtol 1e-3`
 472 `-ksp_pc_side right -ksp_type hpddm -ksp_gmres_restart 40 -ksp_hpddm_type`
 473 `gmres`. With GCRODR, five vectors are recycled throughout the restarts. The last
 474 option has to be switched with `-ksp_hpddm_type gcrodr -ksp_hpddm_recycle 5`.

475 For pseudo-block methods, again, it will be shown next that the timings are
 476 not satisfactory. Again, GCRODR has the edge over GMRES, both in terms of
 477 iterates, 130 against 171, and in terms of runtime, 20.7 min against 26.3 min. This is
 478 a significant improvement compared to the standard methods, with approximately a
 479 4x speedup. The previous command line options remain unchanged, as HPDDM will
 480 by default switch to the pseudo-block variants when solving systems with multiple
 481 right-hand sides.

482 Eventually, the performance of BGMRES and BGCRODR are evaluated. Block
 483 Krylov methods have higher arithmetic intensities and require more involved kernels
 484 such as block orthogonalizations. They are also more memory demanding, since, for
 485 example, the block Arnoldi process generates block Hessenberg matrices, whose QR
 486 factorizations are costlier to compute using Householder reflectors than plain Hessen-
 487 berg matrices factorized with Givens rotations [16]. For that reason, solving the full
 488 system (4.1) with $p = 779$ right-hand sides is not tractable. Instead, the complete
 489 block of right-hand sides is decomposed into contiguous sub-blocks which are then
 490 solved in sequence. At the beginning of each new cycle, deflation is performed us-
 491 ing a tolerance of 10^{-10} . That is, a rank-revealing QR factorization of the block of
 492 initial residuals is computed, and the Arnoldi process only iterates on blocks of size
 493 $i \in \llbracket 1; p \rrbracket$ such that $R_{ii} \leq 10^{-10} R_{11}$. This is achieved in PETSc using the option
 494 `-ksp_matsolve_block_size p'` , which will then successively solve $\lfloor \frac{p}{p'} \rfloor$ subsystems
 495 with at most p' right-hand sides. The complete set of options now reads `-ksp_rtol`
 496 `1e-3 -ksp_pc_side right -ksp_type hpddm -ksp_gmres_restart 30 -ksp_hpddm`
 497 `_deflation_tol 1e-10 -ksp_matsolve_block_size p' -ksp_hpddm_type bgmres`.
 498 Four different values of p' are used: 390, 195, 98, and 49. This corresponds to re-
 499 spectively 2, 4, 8, and 16 successive subsystem solves. The number of iterations,
 500 summed over all subsystem solves, is respectively 42, 101, 263, and 900. Looking
 501 at these numbers, the configuration $p' = 390$ is the most efficient numerically, as
 502 expected, since it is the one that enlarges the generated Krylov subspace the most
 503 per block Arnoldi iteration. However, this numerical efficiency does not transpose to
 504 algorithmic efficiency. Indeed, the time to solution for the previous four block sizes is
 505 respectively 4.7 min, 3.9 min, 3.8 min, and 5.6 min. This highlights the fact that one
 506 has to carefully pick the number of right-hand sides treated simultaneously. On the
 507 one hand, the higher this number, the faster the convergence. On the other hand, the
 508 lower this number, the cheaper block Krylov kernels are, e.g., block orthogonaliza-
 509 tions. BGCRODR has the advantage of handling both blocking and recycling. This
 510 is of great interest here, since multiple solves with the same coefficient matrix A are

511 performed while traversing all sub-blocks of \mathbf{B} . For one of the two near-optimal con-
 512 figurations with BGMRES, $p' = 98$, we instead now switch to BGCRODR. A single
 513 basis vector is recycled throughout successive solves. However, it is important to
 514 keep in mind that a basis vector in the block Krylov sense is in practice a set of p'
 515 vectors. This is achieved by replacing `-ksp_hpddm_type bgmres` by `-ksp_hpddm_type`
 516 `bgcrodr -ksp_hpddm_recycle 1` in the previous set of options. As expected, the
 517 number of iterations, summed over all subsystem solves, is lowered with respect to
 518 BGMRES. It becomes 166 instead of 263. One could then expect faster timings than
 519 with BGMRES, but this is in practice not the case. The time to solution is indeed
 520 7.0 min, which is a great deterioration of the BGMRES timing: almost 3 min slower.
 521 This will be investigated in the next paragraph.

522 All the obtained results are gathered in Table 1. Results that are extrapolated
 523 are typeset in gray, just to highlight that the figures may slightly vary if complete but
 524 wasteful runs were performed instead. Clearly, the use of block Krylov methods is
 525 highly beneficial for solving efficiently (4.1). The most effective methods, BGMRES
 526 with block size of 98 or 195, exhibit a near 28x speedup with respect to a standard
 527 GMRES implementation which does not use either blocking or recycling. For the
 528 sake of thoroughness, we also report the time needed to setup the restricted additive
 529 Schwarz preconditioner: 1.6 sec. Since the coefficient matrix does not change while
 530 solving (4.1), the preconditioner is only computed once, so this timing, compared to
 531 the ones from Table 1, is negligible.

Krylov method	# of blocks	# of RHS/block	$\sum(\# \text{ of iterates})$
GMRES(40)	779	1	153,463
GCRODR(40, 5)	779	1	97,375
P-BGMRES	1	779	171
P-BGCRODR	1	779	130
	16	49	900
BGMRES(30)	8	98	263
	4	195	101
	2	390	42
BGCRODR(30, 1)	8	98	166

Krylov method	Time	/RHS	Speedup
GMRES(40)	1.8 h	8.3 sec	—
GCRODR(40, 5)	1.4 h	6.4 sec	1.3
P-BGMRES	26.3 min	2.0 sec	4.1
P-BGCRODR	20.7 min	1.6 sec	5.2
	5.6 min	0.43 sec	19.3
BGMRES(30)	3.8 min	0.29 sec	28.6
	3.9 min	0.30 sec	27.6
	4.7 min	0.36 sec	23.0
BGCRODR(30, 1)	7.0 min	0.53 sec	15.7

Table 1: Comparison of GMRES, GCRODR, their pseudo-block variant, and their block variant, for solving (4.1) on 960 processes using a restricted additive Schwarz preconditioner

532 **4.3. Pushing forward recycling block Krylov methods.** Though recycling
 533 block Krylov methods have been used successfully in the past [32], results shown
 534 in the previous section are not encouraging. There is at least one explanation for
 535 this discrepancy. Previous studies, e.g., [8, 38], deal with rather moderate num-
 536 bers of right-hand sides, in the hundreds. In the present work, there is one order
 537 of magnitude more vectors, in the thousands. Thus, all algebraic operations from
 538 BGCRODR that scale superlinearly with the dimension of the Krylov subspace are
 539 difficult to amortize. Indeed, these operations are often done redundantly by each
 540 process. Similar considerations apply to, for example, GMRES, where Hessenberg
 541 matrices generated by the Arnoldi process are stored redundantly by each process,
 542 at least as implemented in PETSc, Trilinos [20] and more specifically its Belos pack-
 543 age [5], and HPDDM. In order to alleviate this severe limitation, we propose to redis-
 544 tribute the standard (resp. generalized) eigenvalue problem from BGCRODR line 14
 545 (resp. 31) on a small subset of $N' < N$ processes. This is achieved using the PETSc
 546 option `-ksp_hpddm_recycle_redistribute N'` . Then, the “small” dense distributed
 547 operators are passed to SLEPc [19], which is used to solve the problem instead of
 548 using sequential LAPACK routines redundantly. The computed eigenvectors are then
 549 broadcast to the other $N - N'$ processes.

Krylov method	# of blocks	# of RHS/block
GMRES(40)	779	1
BGMRES(30)	8	98
Naive BGCRODR(30, 1)	4	195
BGCRODR(30, 1)	8	98
BGCRODR(30, 1) + $N' = 9$	4	195

Krylov method	Time	/RHS	Speedup
GMRES(40)	1.8 h	8.3 sec	—
BGMRES(30)	3.8 min	0.29 sec	28.6
Naive BGCRODR(30, 1)	3.9 min	0.30 sec	27.6
BGCRODR(30, 1)	7.0 min	0.53 sec	15.7
BGCRODR(30, 1) + $N' = 9$	2.6 min	0.20 sec	41.5
	3.1 min	0.24 sec	34.6

Table 2: Improvements of the proposed methodology over previous results from Table 1

550 This redistribution scheme has the advantage that not all N processes used for
 551 solving (4.1) will be involved in the eigensolves. The parallel granularity of this
 552 workload is way too fine: solving dense eigenproblems with a few thousand un-
 553 knowns on thousands of processes is likely to perform very poorly due to the very
 554 high communication-to-computation ratio. There is also no available computational
 555 routine in distributed dense linear algebra libraries such as ScaLAPACK for nonsym-
 556 metric eigenproblems. With SLEPc, we instead use the Krylov–Schur method [36],
 557 coupled either by a shift or a shift-and-invert spectral transformation. In this spectral
 558 transformation, an exact distributed LU factorization is computed by Elemental [28]
 559 with the following option `-ksp_hpddm_recycle_mat_type elemental`. This strategy

560 is investigated next with a small communicator of size $N' = 9$. In the previous section,
 561 calls to LAPACK for recycling information took 4.5 min, which explains why the naive
 562 BGCRODR implementation was not competitive against BGMRES. With this new
 563 distributed strategy, again with $p' = 98$, only 6.4 sec are spent in `EPSSolve`, `SLEPc`
 564 computational routine for solving eigenproblems. Even if the recycled information is
 565 now computed iteratively, instead of directly with LAPACK, the overall convergence
 566 of BGCRODR is not impacted, and it still takes 166 iterations to solve all sub-blocks.
 567 However, the time to solution is now 2.6 min. This is more competitive than the pre-
 568 vious BGMRES timing of 3.8 min, and it also makes recycling much more affordable
 569 than in the naive BGCRODR implementation which converged in 7.0 min. The most
 570 efficient strategy has a 41x speedup with respect to a standard GMRES implementa-
 571 tion which does not use blocking. With this efficient BGCRODR implementation, the
 572 case $p' = 195$ is also investigated. The time spent in `EPSSolve` now becomes 18.0 sec,
 573 so the effect of the number of right-hand sides in the sub-block is clearly highlighted.
 574 The number of iterations (resp. time to solution) is now 70 (resp. 3.1 min), which is
 575 indeed less than with BGMRES, but still does not beat BGCRODR with $p' = 98$.
 576 These results are gathered in [Table 2](#), where the first, sixth, seventh, and last row
 577 of [Table 1](#) are recalled first.

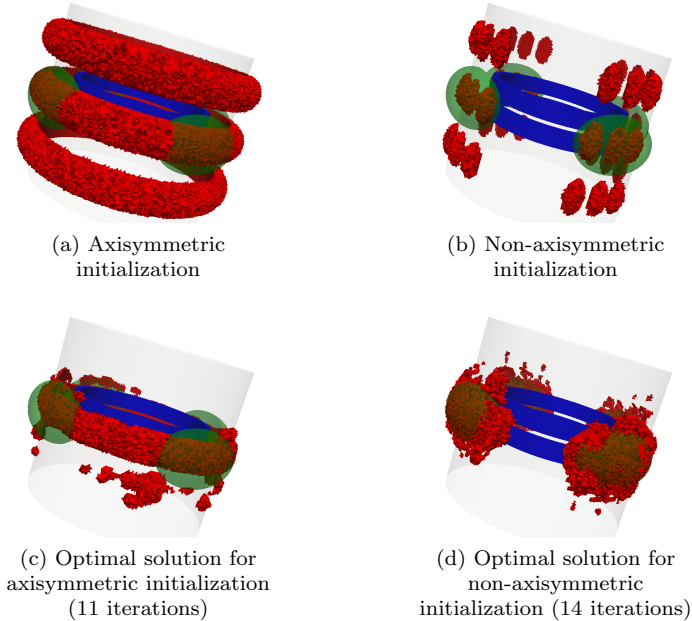


Fig. 5: Convergence results for the SAX probe (in blue) for a target of four ellipsoids (in green) on 960 processes and different shapes of deposits (in red)

578 **5. Deposit reconstruction.** In the previous section, we defined block iterative
 579 solvers that efficiently deal with the direct problem (2.5) for a large number of source
 580 terms. These strategies are investigated now inside the full inverse algorithm. Indeed,
 581 at each iteration, two block systems have to be solved: one for the direct and one for
 582 the adjoint state. Given the large numbers of right-hand sides and of finite element

583 unknowns, the solution phase is bound to be limiting factor per iteration. Let us
 584 illustrate this point with the following test case.

585 We consider synthetic input data, generated numerically. To avoid any bias in the
 586 measurements, the deposit is explicitly defined in the computational mesh to generate
 587 the input data. The target shape here is composed of four ellipsoids at angles 0 , $\pi/2$, π ,
 588 and $3\pi/2$, of z -radius 3.25 mm, r -radius 2.5 mm, and θ -radius 5 mm. We consider here
 589 that the probe scans 41 positions in the z -axis. For solving all systems from [Figure 4](#),
 590 we use the optimal parameters found in the previous section, i.e., BGRODDR with a
 591 single recycled multivector and sub-blocks of size at most 98, see the before last line
 592 from [Table 2](#).

593 Let us first recall the algorithm using a SAX probe. It has only two probes
 594 and generates two signals: one differential and one absolute mode. Therefore, for
 595 one inversion iteration, there are 82 source terms for the direct problem, and as
 596 many terms for the adjoint problem. As such, we expect the resolution of the finite
 597 element problems to be faster than for the SMX probe. We consider two initializations,
 598 displayed in [Figure 5](#).

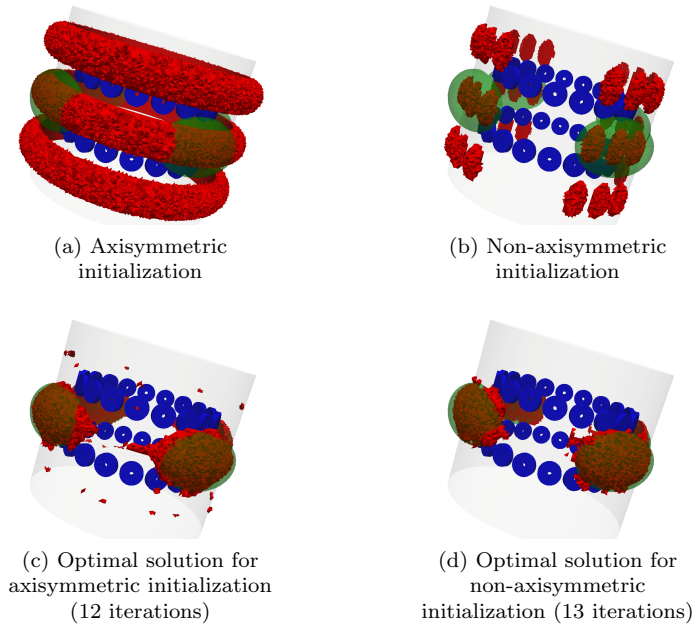


Fig. 6: Convergence results for the SMX probe (in blue) for a target of four ellipsoids (in green) on 960 processes and different shapes of deposits (in red)

599 The convergence plots demonstrate the limits of the SAX probe. As the two coils
 600 of the probe have the same revolution axis as the tube, the information computed
 601 is averaged on the azimuthal component. As a consequence, when initializing the
 602 algorithm with an axisymmetric deposit like in [Figure 5a](#), the optimal shape remains
 603 axisymmetric, see [Figure 5c](#), and does not correspond to the target shape. However,
 604 by choosing a more accurate initialization, e.g., [Figure 5b](#), where we limit the initial-
 605 ization on a domain around the target shape, the inversion loop reconstructs valid
 606 deposits in [Figure 5d](#). Indeed, the optimal solution is now non-axisymmetric. In

607 an industrial context, where we do not know much a priori about the deposit, non-
 608 axisymmetric initializations cannot be considered as they might miss some deposits.
 609 Axisymmetric initializations are preferred as they do not introduce bias in the target
 610 shape. Note that the optimal solution contains small artefacts due to the initialization
 611 that does not vanish through the convergence. However, these artefacts barely influ-
 612 ence the impedance signal. Furthermore, they could be removed by adding constraints
 613 to the optimization problem, for instance surface penalization.

Type of probe	SAX	SMX
Level-set convection	214 sec	2.9 min
Direct solve	14 sec	2.6 min
Adjoint solve	14 sec	2.6 min
Gradient computation	151 sec	7.5 min
Total	436 sec	17 min

Table 3: Different operations for one iteration in the inversion algorithm on 960 processes. The most time-consuming operation is typeset in bold

614 Let us now compare these results with the reconstruction algorithm using the
 615 SMX probe. The probe is made of 38 coils and generates 76 signals: the emitters are
 616 coils on the lower row, each emitter is associated with four receivers on both rows.
 617 As such, the direct problem has 779 source terms, for a problem with approximately
 618 two million finite element unknowns. These figures are the same as in [section 4](#). We
 619 test the same initializations as displayed in [Figure 6](#).

620 In terms of performance, the method with SMX (resp. SAX) converged in about
 621 5 hours (resp. 1 hour and 27 minutes), in 13 iterations, at a rate of about 27 (resp. 8)
 622 minutes per iteration when the descent is accepted, and 7 (resp. 4) minutes per iter-
 623 ation when the descent is rejected. In the latter case, the computation of the adjoint
 624 state and the gradient is skipped. [Table 3](#) summarizes the computational time of the
 625 most demanding operations for one iteration of the inversion algorithm for the two
 626 types of probe.

627

628 Thanks to the use of block Krylov methods, the time spent in both solves is
 629 roughly similar to the time spent in other operations. Compared to the computational
 630 time of about one hour with standard methods like GMRES or GCRODR, see [Table 1](#),
 631 this is a substantial improvement.

632 When comparing the results with the SAX and SMX probes, it appears quite
 633 easily that the computations with the former are faster since the number of source
 634 terms does not exceed a hundred, compared to the 779 RHS of the latter. However,
 635 when comparing the convergence results, it appears that the SMX probe provides
 636 more interesting information on the target deposit.

637 Note that due to the fast resolution of the finite element problems, the remaining
 638 limiting operations are the level-set convection and the gradient computation. The
 639 first operation is currently done sequentially, but can be easily parallelized. For the
 640 second operation, the gradient is computed directly inside FreeFEM domain-specific
 641 language. It could be made more efficient by offloading this operation to a specific
 642 kernel written in a lower-level language, e.g., C++, but this goes beyond the scope of
 643 this paper.

644 **6. Conclusion.** We proposed a complete efficient strategy to solve realistic ECT
 645 for the reconstruction of deposits inside SG. Using a classical least squares formulation
 646 of the inverse problem, the main challenges are:

- 647 • use a formulation of the eddy-current problem that does not require remeshing
- 648 and is independent from the topology of the conductor;
- 649 • use an adapted topological shape optimization method;
- 650 • design an efficient solution strategy that allows for a reasonable inversion
- 651 time.

652 We proposed for the first one the use of a potential formulation combined with rewrit-
 653 ing the problem in terms of scattered field. For the second point, a level-set method
 654 is used combined with appropriate regularization of the descent direction. The bot-
 655 tleneck of the inversion algorithm is the third point where the issue was to efficiently
 656 handle large-scale problems with a large number of RHS. Domain decomposition-
 657 preconditioned Krylov methods proved to be a tool of choice in this case. We com-
 658 pared two different block Krylov algorithms: BGMRES and BGCRODR. We proposed
 659 for the latter a new redistribution scheme to increase its performance. This part is
 660 quite general and may be applied to other large-scale inverse problems. In terms
 661 of deposit reconstructions, though the SAX probe offers less costly computations, it
 662 may fail to reconstruct properly the deposit. In contrast, the SMX probe contains
 663 more information and leads to satisfying results. Thanks to block Krylov methods,
 664 we are able to converge in less than 5 h for a typical industrial problem. Additional
 665 accelerations of the inversion scheme can be obtained by further optimizing the shape
 666 convection step or the computation of the gradient with FreeFEM. These issues will
 667 be explored in a future work where we would like to apply the inversion scheme on
 668 experimental data. Reconstructing at the same time the deposit shape, the material
 669 properties and other possible defects (manufacturing defects, cracks, etc.) is also a
 670 future perspective of this work where the use of a larger set of data may be needed.

671 **Acknowledgments.** This work was granted access to the GENCI-sponsored
 672 HPC resources of TGCC@CEA under allocation A0070607519.

673 REFERENCES

- 674 [1] G. ALLAIRE, F. DE GOURNAY, F. JOUVE, AND A.-M. TOADER, *Structural optimization using*
 675 *topological and shape sensitivity via a level set method*, Control and cybernetics, 34 (2005),
 676 p. 59.
- 677 [2] P. AMESTOY, I. DUFF, J.-Y. L'EXCELLENT, AND J. KOSTER, *A fully asynchronous multifrontal*
 678 *solver using distributed dynamic scheduling*, SIAM Journal on Matrix Analysis and Appli-
 679 cations, 23 (2001), pp. 15–41, <http://mumps.enseiht.fr>.
- 680 [3] S. BALAY, S. ABHYANKAR, M. F. ADAMS, J. BROWN, P. BRUNE, K. BUSCHELMAN, L. DALCIN,
 681 A. DENER, V. ELJKHOUT, W. D. GROPP, D. KARPEYEV, D. KAUSHIK, M. G. KNEPLEY,
 682 D. A. MAY, L. C. MCINNES, R. T. MILLS, T. MUNSON, K. RUPP, P. SANAN, B. F. SMITH,
 683 S. ZAMPINI, H. ZHANG, AND H. ZHANG, *PETSc users manual*, Tech. Report ANL-95/11 -
 684 Revision 3.13, Argonne National Laboratory, 2020.
- 685 [4] S. BALAY, S. ABHYANKAR, M. F. ADAMS, J. BROWN, P. BRUNE, K. BUSCHELMAN, L. DALCIN,
 686 A. DENER, V. ELJKHOUT, W. D. GROPP, D. KARPEYEV, D. KAUSHIK, M. G. KNEPLEY,
 687 D. A. MAY, L. C. MCINNES, R. T. MILLS, T. MUNSON, K. RUPP, P. SANAN, B. F. SMITH,
 688 S. ZAMPINI, H. ZHANG, AND H. ZHANG, *PETSc web page*. <http://www.mcs.anl.gov/petsc>,
 689 2020.
- 690 [5] E. BAVIER, M. HOEMMEN, S. RAJAMANICKAM, AND H. THORNQUIST, *Amesos2 and Belos: Direct*
 691 *and Iterative Solvers for Large Sparse Linear Systems*, Scientific Programming, 20 (2012),
 692 pp. 241–255.
- 693 [6] C. BUI, C. DAPOGNY, AND P. FREY, *An accurate anisotropic adaptation method for solving*
 694 *the level set advection equation*, International Journal for Numerical Methods in Fluids,

```

1:  $R_0 = B_i - AX_0$ 
2: if  $U_k$  is defined (from solving a previous sub-block) then
3:    $[Q, R] = \text{distributed qr}(AU_k)$ 
4:    $C_k = Q$ 
5:    $U_k = U_k R^{-1}$ 
6:    $X_1 = X_0 + U_k C_k^H R_0$ 
7:    $R_1 = R_0 - C_k C_k^H R_0$ 
8: else
9:    $[V_1, S_1] = \text{distributed qr}(R_0)$ 
10:  perform  $m$  steps of BGMRES, thus generating  $V_{m+1}$  and  $[Q, R] = \text{qr}(\overline{H}_m)$  (Arnoldi basis and Hessenberg matrix)
11:  find  $Y_m$  such that  $RY_m = Q^{-1} \begin{bmatrix} S_1 \\ 0_{p \cdot (m-1) \times p} \end{bmatrix}$ 
12:   $X_1 = X_0 + V_m Y_m$ 
13:   $R_1 = B_i - AX_1$ 
14:  solve  $\left( H_m + QR^{-H} \begin{bmatrix} 0_{p \cdot (m-1) \times p \cdot (m-1)} & 0_{p \cdot (m-1) \times p} \\ 0_{p \times p \cdot (m-1)} & h_{m+1, m}^H h_{m+1, m} \end{bmatrix} \right) z_\lambda = \theta_\lambda z_\lambda$ 
15:  store the  $k$  eigenvectors  $z_\lambda$  associated to the smallest eigenvalues in magnitude in  $P_k$ 
16:   $[Q, R] = \text{qr}(\overline{H}_m P_k)$ 
17:   $C_k = V_{m+1} Q$ 
18:   $U_k = V_m P_k R^{-1}$ 
19: end if
20:  $j = 1$ 
21: while convergence not reached do
22:    $[V_k, S_k] = \text{distributed qr}(R_j)$ 
23:    $j += 1$ 
24:   perform  $m-k$  steps of BGMRES with the linear operator  $(I - C_k C_k^H)A$ , thus generating  $V_{m+1-k}$ ,  $[Q, R] = \text{qr}(\overline{H}_{m-k})$ , and  $E_k = C_k A V_{m-k}$ 
25:   find  $Y_{m-k}$  such that  $RY_{m-k} = Q^{-1} \begin{bmatrix} S_k \\ 0_{p \cdot (m-k-1) \times p} \end{bmatrix}$ 
26:    $Y_k = C_k^H R_{j-1} - E_k Y_{m-k}$ 
27:    $X_j = X_{j-1} + U_k Y_k + V_{m-k} Y_{m-k}$ 
28:    $R_j = B_i - AX_j$ 
29:   scale the columns of  $U_k$  so that they are of unit norm and store the scaling coefficients in  $D_k$ 
30:   define  $G_m = \begin{bmatrix} D_k & E_k \\ 0_{p \cdot (m-k+1) \times p \cdot k} & \overline{H}_{m-k} \end{bmatrix}$ 
31:   solve  $G_m^H G_m z_\lambda = \theta_\lambda G_m^H \left( \begin{bmatrix} C_k^H U_k & 0_{p \cdot k \times p \cdot (m-k)} \\ V_{m-k+1}^H U_k & I_{p \cdot (m-k+1) \times p \cdot (m-k)} \end{bmatrix} \right) z_\lambda$ 
32:   store the  $k$  eigenvectors  $z_\lambda$  associated to the smallest eigenvalues in magnitude in  $P_k$ 
33:    $[Q, R] = \text{qr}(\overline{H}_m P_k)$ 
34:    $C_k = \begin{bmatrix} C_k & V_{m-k+1} \end{bmatrix} Q$ 
35:    $U_k = \begin{bmatrix} U_k P_k & V_{m-k} P_k \end{bmatrix} R^{-1}$ 
36: end while

```

Fig. 7: BGCRODR as written by Jolivet and Tournier [23]

- 695 70 (2012), pp. 899–922.
- 696 [7] X.-C. CAI AND M. SARKIS, *A Restricted Additive Schwarz Preconditioner for General Sparse*
697 *Linear Systems*, SIAM Journal on Scientific Computing, 21 (1999), pp. 792–797.
- 698 [8] H. CALANDRA, S. GRATTON, J. LANGOU, X. PINEL, AND X. VASSEUR, *Flexible Variants of Block*
699 *Restarted GMRES Methods with Application to Geophysics*, SIAM Journal on Scientific
700 Computing, 34 (2012), pp. A714–A736.
- 701 [9] M. COSTABEL AND M. DAUGE, *Singularities of electromagnetic fields in polyhedral domains*,
702 *Archive for Rational Mechanics and Analysis*, 151 (2000), pp. 221–276.
- 703 [10] C. DAPOGNY, P. FREY, F. OMNÈS, AND Y. PRIVAT, *Geometrical shape optimization in fluid*
704 *mechanics using FreeFem++*, Structural and Multidisciplinary Optimization, 58 (2018),
705 pp. 2761–2788.
- 706 [11] V. DOLEAN, P. JOLIVET, AND F. NATAF, *An Introduction to Domain Decomposition Methods:*
707 *Algorithms, Theory and Parallel Implementation*, SIAM, 2015.
- 708 [12] O. DORN AND D. LESSELIER, *Level set methods for inverse scattering*, Inverse Problems, 22
709 (2006), p. R67.
- 710 [13] T. DUPUY, *Modélisation des transferts thermiques dans les dépôts d’encrassement des*
711 *générateurs de vapeur*, PhD thesis, Ecole Centrale de Marseille, 2019.
- 712 [14] J. GARCÍA-MARTÍN, J. GÓMEZ-GIL, AND E. VÁZQUEZ-SÁNCHEZ, *Non-destructive techniques*
713 *based on eddy current testing*, Sensors, 11 (2011), pp. 2525–2565.
- 714 [15] M. H. GUTKNECHT, *Block Krylov space methods for linear systems with multiple right-hand*
715 *sides: an introduction*, in Modern Mathematical Models, Methods and Algorithms for Real
716 World Systems, A. Siddiqui, I. Duff, and O. Christensen, eds., 2006, pp. 420–447.
- 717 [16] M. H. GUTKNECHT AND T. SCHMELZER, *Updating the QR decomposition of block tridiagonal*
718 *and block Hessenberg matrices*, Applied Numerical Mathematics, 58 (2008), pp. 871–883.
- 719 [17] H. HADDAR, Z. JIANG, AND M. K. RIAHI, *A robust inversion method for quantitative 3d shape*
720 *reconstruction from coaxial eddy current measurements*, Journal of Scientific Computing,
721 70 (2017), pp. 29–59.
- 722 [18] F. HECHT, *New development in FreeFem++*, Journal of numerical mathematics, 20 (2012),
723 pp. 251–266.
- 724 [19] V. HERNANDEZ, J. E. ROMAN, AND V. VIDAL, *SLEPc: A scalable and flexible toolkit for the*
725 *solution of eigenvalue problems*, ACM Transactions on Mathematical Software, 31 (2005),
726 pp. 351–362, <https://slepc.upv.es>.
- 727 [20] M. A. HEROUX, R. A. BARTLETT, V. E. HOWLE, R. J. HOEKSTRA, J. J. HU, T. G. KOLDA,
728 R. B. LEHOUCQ, K. R. LONG, R. P. PAWLOWSKI, E. T. PHIPPS, ET AL., *An overview of*
729 *the Trilinos project*, ACM Transactions on Mathematical Software (TOMS), 31 (2005),
730 pp. 397–423, <https://trilinos.github.io>.
- 731 [21] Z. JIANG, H. HADDAR, A. LECHLEITER, AND M. EL-GUEDRI, *Identification of magnetic de-*
732 *posits in 2-d axisymmetric eddy current models via shape optimization*, Inverse Problems
733 in Science and Engineering, 24 (2016), pp. 1385–1410.
- 734 [22] P. JOLIVET, J. E. ROMAN, AND S. ZAMPINI, *KSPHPDDM and PCHPDDM: Extending PETSc*
735 *with robust overlapping Schwarz preconditioners and advanced Krylov methods*, submitted for
736 publication, (2020), <https://github.com/prj-/jolivet2020petsc>.
- 737 [23] P. JOLIVET AND P.-H. TOURNIER, *Block Iterative Methods and Recycling for Improved Scal-*
738 *ability of Linear Solvers*, in Proceedings of the 2016 International Conference for High
739 Performance Computing, Networking, Storage and Analysis, SC16, IEEE, 2016.
- 740 [24] L. MAURICE, V. COSTAN, E. GUILLOT, AND P. THOMAS, *Eddy current NDE performance*
741 *demonstrations using simulation tools*, in AIP Conference Proceedings, vol. 1511, American
742 Institute of Physics, 2013, pp. 464–471.
- 743 [25] S. OSHER, R. FEDKIW, AND K. PIECHOR, *Level set methods and dynamic implicit surfaces*,
744 *Appl. Mech. Rev.*, 57 (2004), pp. B15–B15.
- 745 [26] T. P. AND G. B., *La simulation des CND-CF complexes a la portée des ingénieurs*, in Pro-
746 ceedings of the 2017 Journées COFREND, Modélisation courants de Foucault, COFREND,
747 2017.
- 748 [27] M. L. PARKS, E. DE STURLER, G. MACKAY, D. D. JOHNSON, AND S. MAITI, *Recycling Krylov*
749 *Subspaces for Sequences of Linear Systems*, SIAM Journal on Scientific Computing, 28
750 (2006), pp. 1651–1674.
- 751 [28] J. POULSON, B. MARKER, R. A. VAN DE GEIJN, J. R. HAMMOND, AND N. A. ROMERO, *El-*
752 *emental: A new framework for distributed memory dense matrix computations*, ACM
753 Transactions on Mathematical Software, 39 (2013).
- 754 [29] T. PRUSEK, *Modélisation et simulation numérique du colmatage à l’échelle du sous-canal dans*
755 *les générateurs de vapeur*, PhD thesis, Aix-Marseille, 2012.
- 756 [30] M. K. RIAHI, *A fast eddy-current non destructive testing finite element solver in steam gener-*

- 757 *ator*, Journal of Coupled Systems and Multiscale Dynamics, 4 (2016), pp. 60–68.
- 758 [31] A. A. RODRÍGUEZ AND A. VALLI, *Eddy current approximation of Maxwell equations: theory,*
759 *algorithms and applications*, vol. 4, Springer Science & Business Media, 2010.
- 760 [32] F.-X. ROUX AND A. BARKA, *Block Krylov recycling algorithms for FETI-2LM applied to 3D*
761 *electromagnetic wave scattering and radiation*, IEEE Transactions on Antennas and Prop-
762 *agation*, 65 (2017), pp. 1886–1895.
- 763 [33] Y. SAAD AND M. H. SCHULTZ, *GMRES: A generalized minimal residual algorithm for solving*
764 *nonsymmetric linear systems*, SIAM Journal on Scientific and Statistical Computing, 7
765 (1986), pp. 856–869.
- 766 [34] M. SCHWEIGER, S. ARRIDGE, O. DORN, A. ZACHAROPOULOS, AND V. KOLEHMAINEN, *Recon-*
767 *structing absorption and diffusion shape profiles in optical tomography by a level set tech-*
768 *nique*, Optics letters, 31 (2006), pp. 471–473.
- 769 [35] B. F. SMITH, P. BJØRSTAD, AND W. D. GROPP, *Domain decomposition: parallel multilevel*
770 *methods for elliptic partial differential equations*, Cambridge University Press, 2004.
- 771 [36] G. W. STEWART, *A Krylov–Schur Algorithm for Large Eigenproblems*, SIAM Journal on Matrix
772 *Analysis and Applications*, 23 (2002), pp. 601–614.
- 773 [37] A. TOSELLI AND O. B. WIDLUND, *Domain decomposition methods: algorithms and theory*,
774 vol. 34 of Series in Computational Mathematics, Springer, 2005.
- 775 [38] P.-H. TOURNIER, I. ALIFERIS, M. BONAZZOLI, M. DE BUHAN, M. DARBAS, V. DOLEAN,
776 F. HECHT, P. JOLIVET, I. EL KANFOUD, C. MIGLIACCIO, F. NATAF, C. PICHOT, AND
777 S. SEMENOV, *Microwave Tomographic Imaging of Cerebrovascular Accidents by Using*
778 *High-Performance Computing*, Parallel Computing, 85 (2019), pp. 88–97.
- 779 [39] M. Y. WANG, X. WANG, AND D. GUO, *A level set method for structural topology optimization*,
780 *Computer methods in applied mechanics and engineering*, 192 (2003), pp. 227–246.
- 781 [40] G. ZENZINGER, J. BAMBERG, W. SATZGER, AND V. CARL, *Thermographic crack detection by*
782 *eddy current excitation*, Nondestructive Testing and Evaluation, 22 (2007), pp. 101–111.